ACS Catalysis
Research Article
pubs.acs.org/acscatalysis

Intermetallic $GaPd_2$ Nanoparticles on SiO_2 for Low-Pressure CO_2 Hydrogenation to Methanol: Catalytic Performance and In Situ Characterization

Elisabetta M. Fiordaliso,*[,†] Irek Sharafutdinov,[‡] Hudson W. P. Carvalho,[§] Jan-D. Grunwaldt,[∥] Thomas W. Hansen,[†] Ib Chorkendorff,[‡] Jakob B. Wagner,[†] and Christian D. Damsgaard[†,‡]

[†]Center for Electron Nanoscopy, [‡]Center for Individual Nanoparticle Functionality, Department of Physics, Technical University of Denmark, DK-2800 Lyngby, Denmark

[§]Centro de Energia Nuclear na Agricultura, Universidade de São Paulo, P.O. Box 96, 13400-970, Piracicaba, SP, Brazil

[∥]Institute for Chemical Technology and Polymer Chemistry, Karlsruhe Institute of Technology, Engesserstrasse 20, D-76131 Karlsruhe, Germany

Supporting Information

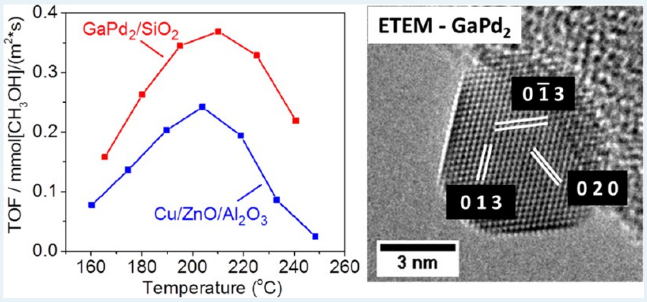

ABSTRACT: A nanodispersed intermetallic $GaPd_2/SiO_2$ catalyst is prepared by simple impregnation of industrially relevant high-surface-area SiO_2 with Pd and Ga nitrates, followed by drying, calcination, and reduction in hydrogen. The catalyst is tested for CO_2 hydrogenation to methanol at ambient pressure, revealing that the intrinsic activity of the $GaPd_2/SiO_2$ is higher than that of the conventional $Cu/ZnO/Al_2O_3$, while the production of the undesired CO is lower. A combination of complementary in situ and ex situ techniques are used to investigate the $GaPd_2/SiO_2$ catalyst. In situ X-ray diffraction and in situ extended X-ray absorption fine structure spectroscopy show that the $GaPd_2$ intermetallic phase is formed upon activation of the catalyst via reduction and remains stable during CO_2 hydrogenation. Identical location−transmission electron microscopy images acquired ex situ (i.e., micrographs of exactly the same catalyst area recorded at the different steps of activation and reaction procedure) show that nanoparticle size and dispersion are defined upon calcination with no significant changes observed after reduction and methanol synthesis. Similar conclusions can be drawn from electron diffraction patterns and images acquired using environmental TEM (ETEM), indicating that ETEM results are representative for the catalyst treated at ambient pressure. The chemical composition and the crystalline structure of the nanoparticles are identified by scanning TEM energy dispersive X-ray spectroscopy, selected area electron diffraction, and atomically resolved TEM images.

KEYWORDS: *methanol synthesis, intermetallics, in situ characterization, XRD, TEM, EXAFS*

1. INTRODUCTION

Methanol is a bulk chemical produced in several million tons per year used as the basis for many important downstream products, such as formaldehyde, acetic acid, and plastics.[1] Methanol can be used as a direct fuel[2] or converted into products with a high calorific value, such as dimethyl ether[3,4] or hydrocarbons.[5−7] Traditionally, methanol is produced from syngas, that is, a mixture of H_2, CO, and CO_2, on highly optimized $Cu/ZnO/Al_2O_3$ catalysts at temperatures up to 300 °C and pressures up to 100 bar.[8−13] The major drawback of the copper-based catalysts is sintering, which leads to severe deactivation.[14−16]

As an alternative, methanol can be produced by hydrogenation of CO_2, according to eq 1.

$$CO_2 + 3H_2 \rightleftharpoons CH_3OH + H_2O \quad (1)$$

Hydrogenation of CO_2 to methanol has been attracting continuous worldwide research interest because of its positive environmental impact, and it is proposed as the basis of the so-called "methanol economy".[17] However, a catalyst giving a high CH_3OH-to-CO ratio has to be developed to make the process more feasible. Moreover, to achieve the "methanol economy", methanol has to be produced in decentralized units, where a catalyst optimized for operating at low pressure is required.

Attempts have been made to optimize the conventional $Cu/ZnO/Al_2O_3$ catalyst for CO_2 hydrogenation,[18,19] with the major challenge being suppressing the reverse water gas shift (rWGS) reaction described by eq 2.

$$CO_2 + H_2 \rightleftharpoons CO + H_2O \quad (2)$$

Recently, Ni−Ga intermetallics have been proposed as catalysts for ambient pressure CO_2 hydrogenation to methanol.[20]

Received: June 16, 2015
Revised: August 27, 2015
Published: August 27, 2015

DOI: 10.1021/acscatal.5b01271
ACS Catal. 2015, 5, 5827−5836

Catalytic tests show that δ-Ni_5Ga_3/SiO_2 is the most active among the Ni−Ga intermetallics, but it suffers from deactivation due to carbon poisoning.[20,21]

Pd−Ga intermetallic compounds, especially the $GaPd_2$ phase, have also been reported as highly active and selective for methanol synthesis from CO_2.[22−26] Various methods for preparation of both unsupported and supported Pd−Ga intermetallic compounds have been suggested. These include synthesis of the bulk phase from pure metals,[27] preparation of unsupported nanoparticles by grinding the bulk phase,[28] coprecipitation,[23,29] impregnation,[30−32] and a colloidal approach.[33,34]

In this study, a simple method for preparation of highly dispersed $GaPd_2$ nanoparticles on an industrially relevant high surface area SiO_2 support is described. The intrinsic activity, selectivity, and stability of the $GaPd_2/SiO_2$ catalyst at ambient pressure are compared with the conventional $Cu/ZnO/Al_2O_3$ catalyst. A combination of complementary techniques is used to characterize the catalyst during nanoparticle formation and methanol synthesis. In situ X-ray diffraction (XRD) and in situ extended X-ray absorption fine structure (EXAFS) analysis are used to determine the long-range crystal structure and local structure of the catalyst, respectively. Particle formation and evolution are monitored ex situ by identical location−transmission electron microscopy (IL-TEM) and in situ by environmental TEM (ETEM) at a total pressure of 4 mbar. The chemical composition and the crystalline structure of the $GaPd_2/SiO_2$ nanoparticles are identified by scanning transmission electron microscopy (STEM) energy dispersive X-ray apectroscopy (EDX), selected area electron diffraction (SAED), and atomically resolved TEM.

2. EXPERIMENTAL SECTION

2.1. Catalyst Preparation. $GaPd_2/SiO_2$ (23 wt % of metals) catalysts were prepared by incipient wetness impregnation of high-surface-area SiO_2 (241 m^2/g, Saint-Gobain Norpro) with a solution of $Pd(NO_3)_2$ (Carl Roth GmbH) and $Ga(NO_3)_3$ (Sigma-Aldrich, 99.9%) in 4 M HNO_3. For comparison, a conventional $Cu/ZnO/Al_2O_3$ catalyst was prepared following the procedures described in ref 35. The choice of metal loading was dictated by normalization considerations, making sure that the total amount of metals (Pd and Ga) in moles was the same as in the $Cu/ZnO/Al_2O_3$ (48 wt % of Cu) catalyst. The amount of catalyst used was 0.167 g of $Cu/ZnO/Al_2O_3$ and 0.514 g of $GaPd_2/SiO_2$. To ensure consistency in the specific velocities during testing of the two catalysts, the $Cu/ZnO/Al_2O_3$ catalyst was diluted with inert SiC to match the volume of the $GaPd_2/SiO_2$.

A catalyst preparation and testing scheme was developed, consisting of four stages: drying, calcination, reduction, and reaction. The procedure was adapted from ref 32 with some modifications. Initially, the catalyst precursor was dried and calcined under static air at 120 °C (overnight) and 260 °C (4 h), then the precursor was heated to 550 °C in a flow of 25% H_2/Ar at ambient pressure, with a heating rate of 5 °C/min. After reducing the catalyst for 2 h, the temperature was decreased to 165 °C for catalytic testing.

2.2. Catalytic Tests. Activity measurements were performed at ambient pressure in a quartz glass reactor (d_i = 6 mm) with a catalyst sieve fraction of 0.212−0.354 mm. Total flow rate of the stoichiometric feed gas, CO_2 (25%) and H_2 (75%), was 100 N mL/min, and the catalytic bed volume was 1.13 cm^3. The temperature across the reaction zone was monitored by two thermocouples placed before and after the catalyst bed. An Agilent 7890A gas chromatograph (GC) equipped with thermal conductivity detector (TCD) and flame ionization detector (FID) was used to analyze the reaction mixture. The configuration of the GC is described in detail elsewhere.[21] The product gas was injected every 15 min, and five measurements were carried out at each temperature to ensure stable conversion.

2.3. In Situ X-ray Diffraction. XRD measurements were performed using a PAN-Analytical X'PERT PRO diffractometer equipped with an Anton Paar XRK-900 furnace, using Ni filtered Cu Kα radiation. The furnace was connected to a gas handling system able to provide H_2, CO_2, and inert gases. A sample of high-surface-area silica (SiO_2)-impregnated with $Pd(NO_3)_2$ and $Ga(NO_3)_3$ was converted to $GaPd_2/SiO_2$ following the procedure described in Section 2.1, with the difference that drying and calcination were also performed in situ under a flow of synthetic air at ambient pressure. The methanol synthesis step was carried out for 20 h at 200 °C (because at 200 °C, as will be shown in Section 3.1, methanol production is close to the maximum). XRD patterns were recorded at room temperature after each step of the catalyst preparation and testing scheme, namely, drying of the metal nitrates, calcination, temperature-programmed reduction (TPR), and CO_2 hydrogenation to methanol.

The crystallite size of the supported nanoparticles was determined from Scherrer broadening analysis of the most intense crystallographic reflections in the XRD patterns.

In another experiment, the procedure described above was repeated at a total pressure of 200 mbar, with a partial pressure of 4 mbar of H_2, using He as carrier gas. This was done to verify whether the same active $GaPd_2/SiO_2$ phase is formed in the ETEM, where the total pressure is limited to 4 mbar of H_2.

2.4. Extended X-ray Absorption Fine Structure. In situ EXAFS measurements were carried out at the SAMBA beamline, Soleil Synchrotron facility, France. The spectra were recorded in transmission mode. The synchrotron radiation at this experimental station is provided by a bending magnet. First, two Pd-coated mirrors operating in grazing incidence mode reject the higher harmonics and provide vertical collimation and focus. The X-rays are then monochromatized by channel-cut monochromators: Si(111) was used for Ga−K edge (10.367 eV), and Si(311), for the Pd−K edge (24.350 eV).

The calcined catalyst precursor was loaded in a quartz capillary (d_i = 1.0 mm, wall thickness 0.02 mm) and reduced in a 25% H_2/He mixture by increasing the temperature to 550 °C at a rate of 5 °C/min and a dwell time of 2 h. The temperature was measured by a thermocouple placed directly below the capillary.[36] The EXAFS spectra were recorded at room temperature after cooling under the same reducing atmosphere.

The data analysis was performed using the Athena and Artemis software of the IFEFFIT package.[37] The spectra were energy-calibrated using Pd and W metal foils as references, the data were normalized, and the background was subtracted. Using the atomic positions given by crystallographic data of $GaPd_2$,[38] an atomic cluster was built using the FEFF6.0 code (running within Artemis).[39] Theoretical amplitude and phase shifts for Pd and Ga were calculated. The structural parameters—namely, number of neighbors (N), atomic distances (R), and mean square deviation of interatomic distances (σ^2)—were determined during the refinement of the theoretically calculated spectra with the experimental spectra. The energy misalignment between the theory and experiment was compensated by the energy-shift factor (ΔE_0). The amplitude reduction factor (S_0^2) for Pd was

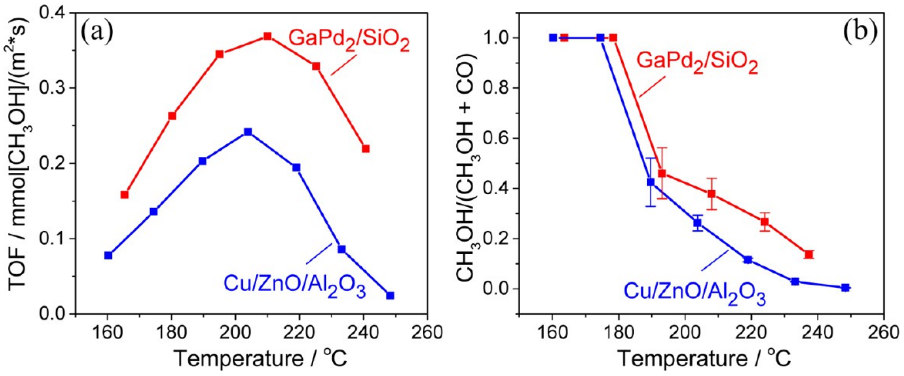

Figure 1. (a) Turnover frequency and (b) CH3OH-to-CO ratio from GaPd$_2$/SiO$_2$ and Cu/ZnO/Al$_2$O$_3$ catalysts as a function of reaction temperature.

obtained by refining the spectrum of a Pd foil, whereas that of Ga was determined from the spectrum of Ga(NO$_3$)$_3$. The fit quality is represented by the ρ-factor, which is the squared difference between the points of the experimental curve and the refined one multiplied by 100. The curve fitting for Pd and Ga spectra was carried out in R-space simultaneously because they share structural parameters. This procedure was performed on the k^2-weigthed Fourier transformed EXAFS spectra (Hanning window) using a k range between 2 and 13 Å^{-1} and R between 1 and 3 Å for both Pd and Ga edges.

2.5. Transmission Electron Microscopy (TEM). *2.5.1. IL-TEM (Ex Situ Characterization).* The identical location TEM method is able to provide a direct, visual observation of structural and compositional changes affecting catalysts along a specific test scheme. The method has proven its efficiency in the characterization of electrocatalysts[40,41] and Fischer−Tropsch synthesis catalysts.[42] In this study, it was used to investigate nanoparticle formation and catalyst evolution. For this purpose, a catalyst precursor, consisting of Pd(NO$_3$)$_2$ and Ga(NO$_3$)$_3$ impregnated onto high-surface-area SiO$_2$, was placed on Au/C TEM grids. The grids were fixed in a custom-made ceramic holder, which was placed into a furnace with a controlled gas atmosphere. In the furnace, the precursor was subjected to drying; calcination; temperature-programmed reduction; and, finally, to reaction gas environment at ambient pressure, as described in Section 2.3. Between steps, the grid was transferred in air to the TEM, where images were acquired. After the reduction step, the catalyst was passivated in 1% O$_2$/Ar mixture at 30 °C for 40 min. Consequently, before carrying out the methanol synthesis reaction step, the catalyst was reactivated in a flow of 25% H$_2$/He at 550 °C.

IL-TEM images were acquired in an FEI Tecnai T20 microscope operating at 200 kV, using a FEI single tilt holder. High-angle annular dark-field scanning TEM (HAADF-STEM) images were acquired using an FEI Titan FEG TEM operated at 120 kV. EDX spectra were recorded using an Oxford silicon drift detector. The local chemical composition of the supported nanoparticles was studied by spot and line scan measurements.

2.5.2. Environmental TEM (In Situ Characterization). ETEM enables real time dynamic studies of heterogeneous catalysts under controlled gas environments and reaction temperatures at limited pressure, generally up to 20 mbar. In this work, the catalyst preparation and testing scheme was reproduced in a total pressure of 4 mbar in a FEI Titan ETEM operating at 300 kV, in which a differential pumping system allows gases to be introduced into the microscope column.[43] The drying and calcining steps were carried out at 120 and 260 °C, respectively, in a N$_2$/O$_2$ mixture of 4:1 for 1 h. The reduction was carried out for 2 h at 550 °C in pure H$_2$, whereas the reaction step was carried out for 2 h at 200 °C in a 3:1 H$_2$/CO$_2$ mixture. The SiO$_2$-supported Pd and Ga nitrate precursor was deposited onto a MEMS (micro electro-mechanical system) heater (Protochips), placed in the Protochips ADURO heating holder. Low magnification images and selected area electron diffraction (SAED) patterns were acquired at the different stages of the catalyst preparation and testing scheme. In addition, atomically resolved images of individual nanoparticles were acquired under reduction conditions.

3. RESULTS AND DISCUSSION

3.1. Catalytic Testing. The turnover frequency (TOF) values corresponding to methanol production from the GaPd$_2$/SiO$_2$ and the Cu/ZnO/Al$_2$O$_3$ catalysts at atmospheric pressure are shown in Figure 1a. The TOF values, (mol$_{\mathrm{CH_3OH}}$)/(m^2 × s), were calculated assuming that the particles are spherical and monocrystalline. The average particle size was estimated from XRD patterns by Scherrer broadening analysis of the crystallographic reflections (020) for the GaPd$_2$ and (111) for the Cu/ZnO/Al$_2$O$_3$, shown in Figure 2. In the case of GaPd$_2$/SiO$_2$, the presence of ~9 wt % of metallic palladium was observed. The amount of unalloyed Pd has been estimated by comparing the relative intensities of the Pd and GaPd$_2$ reflections. The average

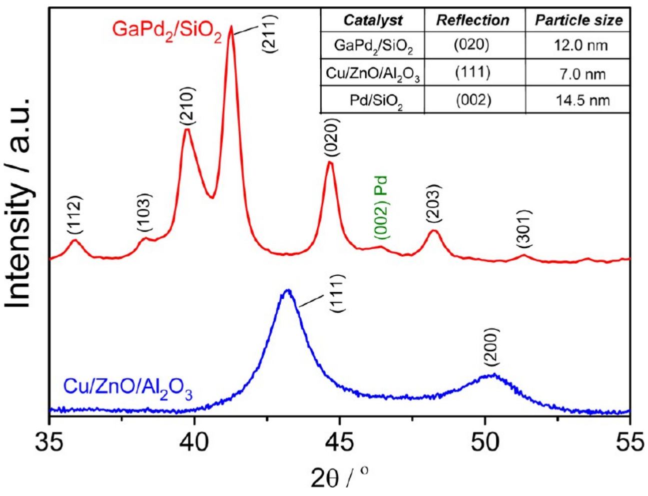

Figure 2. XRD patterns of the GaPd$_2$/SiO$_2$ and the Cu/ZnO/Al$_2$O$_3$ catalysts. The inset shows the particle size estimated by the Scherrer equations.

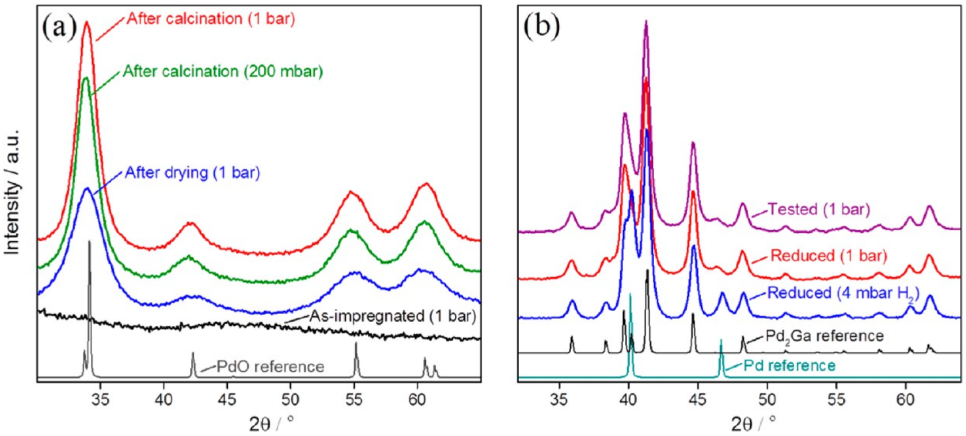

Figure 3. (a) XRD patterns acquired at room temperature and ambient pressure from the as-impregnated, dried, and calcined catalyst precursor and (b) from the reduced and tested for CO_2 hydrogenation $GaPd_2/SiO_2$ catalyst.

size of Pd crystals was estimated to be 14.5 nm. The main Pd reflection (111), at $2\theta = 40.2°$, is masked by the (210) and (211) reflections of $GaPd_2$.

The intrinsic activity of the $GaPd_2/SiO_2$ catalyst for hydrogenation of CO_2 to methanol is found to be higher than that of the $Cu/ZnO/Al_2O_3$ catalyst. It has previously been reported that the activity of the $GaPd_2/Ga_2O_3$ catalyst for this reaction, normalized by active metal content, is 5 times higher at 250 °C and 30 bar compared with the $Cu/ZnO/Al_2O_3$.[29] The TOF of the hydrotalcite-derived $GaPd_2$ catalyst was found to be 2.5 times lower than that of the $Cu/ZnO/Al_2O_3$ under similar conditions, but compared with monometallic Pd catalyst, the activity is 200 times higher.[23]

Here, the intrinsic activity of the $GaPd_2/SiO_2$ catalyst is ~1.6 times higher compared with $Cu/ZnO/Al_2O_3$, showing that an active $GaPd_2$ phase can be prepared by a wetness impregnation method, as well. Furthermore, the intrinsic activity of the $GaPd_2/SiO_2$ catalyst is found to be ~2.0 times higher than novel Ni_5Ga_3/SiO_2 catalysts.[20]

Figure 1b shows that the selectivity toward CH_3OH is twice as high for the $GaPd_2/SiO_2$ system compared with the conventional copper catalyst at 205−210 °C, where the CO_2 conversion is the highest. The lower amount of CO produced by the $GaPd_2/SiO_2$ catalyst not only improves the selectivity but also allows for a higher amount of methanol to be produced as a result of thermodynamic considerations (see the Supporting Information).

The uncertainty in the CH_3OH-to-CO ratio stems from the detection limit of the GC: below 190 °C, the amount of CO approaches the detection limit, and below 170 °C, the measured concentration of CO in the product gas is zero for both catalysts. This is most likely because the amount of CO produced in this temperature regime cannot be detected by the GC used in this work. The detection limit of methanol is, in contrast, 2 orders of magnitude lower than the lowest measured values, which ensures negligible uncertainty in the CH_3OH signal.

The only byproduct formed during the reaction is CO, which is also the case for the $Cu/ZnO/Al_2O_3$ catalyst. Moreover, the activity of the $GaPd_2/SiO_2$ catalyst measured at 200 °C over 20 h is stable (see Supporting Information). This is an improvement compared with the $Cu/ZnO/Al_2O_3$ catalyst, which experiences ~25% of initial activity loss under similar conditions.

These catalytic results demonstrate that the $GaPd_2/SiO_2$ catalyst prepared by simple impregnation of metal nitrates could be an interesting candidate for CO_2 hydrogenation to methanol at ambient pressure. The characterization results show that an important step toward optimization of this catalyst is revealing its structure and formation mechanism.

3.2. Catalyst Characterization. A combination of complementary characterization techniques is used to characterize the catalyst along the catalyst preparation and testing scheme.

3.2.1. In Situ XRD. The XRD patterns acquired at 1 bar at the four steps of the catalyst preparation and testing scheme are shown in Figure 3. Upon drying and calcination, the PdO phase is formed,[44] which is expected upon high temperature treatment of metal nitrates. A significant phase change is observed during reduction of the precursor in the H_2/Ar flow at 550 °C, when the $GaPd_2$ phase is formed. The XRD patterns acquired after preparation and testing steps are presented in Figure 3b. The patterns for $GaPd_2$ and metallic Pd are included as references.[38,45] No changes in the crystal structure or crystallite size are observed upon exposure of the catalyst to reaction conditions, indicating that the bulk structure of the $GaPd_2$ phase is stable. This is important for potential applications because in some cases, such as for NiZn in the methanol steam reforming reaction,[46] the decomposition of the bulk structure of the intermetallic compound is observed.

After reduction at 1 bar, the presence of 9 wt % of metallic Pd is also detected. This value was estimated by comparison of the intensities given by the $GaPd_2$ and Pd reflections. In this work, we have not tested the catalytic activity of monometallic Pd for hydrogenation of CO_2 to methanol because it is reported to be negligible.[23,47] Therefore, the catalytic activity toward methanol formation is attributed solely to the $GaPd_2$ phase. As suggested in ref 23, the unalloyed metallic palladium could be responsible for the CO production in the rWGS reaction. In contrast, other groups[22,25] have demonstrated that metallic palladium supported on SiO_2 or carbon nanotubes has no or little activity toward reduction of CO_2 to CO.

A similar "low pressure" in situ XRD experiment has been carried out under a total pressure of 200 mbar, keeping the partial pressure of H_2 at 4 mbar during the catalyst reduction. This was conducted to mimic the partial pressure of hydrogen in the ETEM (see Section 3.2.4) and justify the direct comparison of the results obtained by the two techniques. It is found that both ambient pressure and "low pressure" in situ XRD lead to the formation of the $GaPd_2$ phases with similar values of the average crystal size, that is, 12.0 and 12.6 nm, respectively, calculated

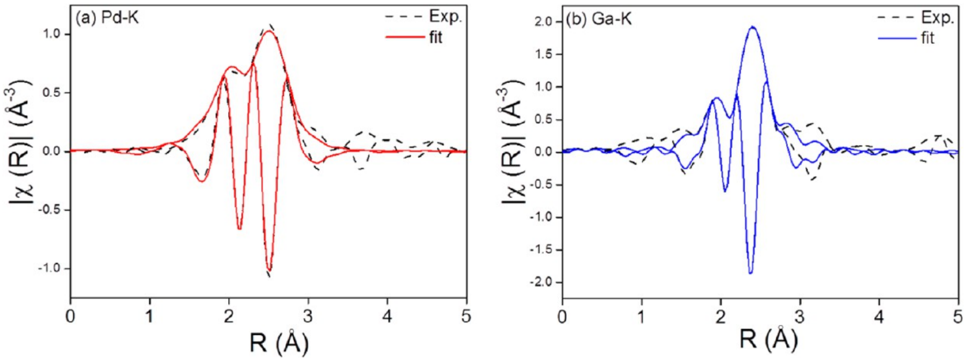

Figure 4. Experimental (dashed lines) and fitted (solid lines) Fourier transformed EXAFS spectra collected at Pd (a) and Ga (b) K-edges. Spectra are recorded at 25 °C under reducing conditions.

Table 1. Structural Parameters Obtained from EXAFS Data Analysis at Pd and Ga K-Edges[a]

edge	shell	atom	N	R (Å)	σ^2 (10^{-3} Å^2)	ΔE_0 (eV)	ρ (%)
Pd K	1st	Ga	3.1 ± 0.6[b,d]	2.52 ± 0.01[b,c]	6.5 ± 0.6[b,c]	−3.3 ± 1.2	2.5
	2nd	Pd	7.5 ± 1.4[b]	2.81 ± 0.02[b]	11.4 ± 2.0[b]		
Ga K	1st	Pd	5.6 ± 0.3[b]	2.52 ± 0.01[b,c]	6.5 ± 0.6[b,c]	2.1 ± 0.4	

[a] Pd S_0^2 = 0.83 and Ga S_0^2 = 0.88. Pd−Pd atomic distance refined for Pd foil was 2.74 Å. [b] Adjusted parameter. [c] Constrained parameter. [d] 10% correction was applied on the basis of XRD results that showed that part of the Pd atoms were not alloyed.

from the broadening of the (020) peak. Moreover, in both cases, PdO crystallites of similar size (i.e. 4.4 and 4.3 nm) are formed after the calcination step.

In the case of the "low pressure" experiment, the content of unalloyed metallic palladium is slightly higher: 15 wt %, in contrast with 9 wt % observed after the ambient pressure reduction, as estimated by comparing the relative intensities of the Pd and $GaPd_2$ reflections. This discrepancy could be due to a longer alloying time required at 4 mbar, stemming from the difference in the flow conditions in the in situ XRD cell when the pressure is reduced from 1 bar to 4 mbar. Nevertheless, the results indicate that the path to formation of the $GaPd_2$ phase is similar irrespective of the pressure. This implies that the as-prepared and tested $GaPd_2/SiO_2$ catalyst, formed in the ETEM at low pressure, should be comparable to the one prepared and tested in a tubular reactor at 1 bar in terms of the structure of the active phase. However, a slight difference in the relative abundance of the $GaPd_2$ and Pd phases might be expected.

The acquired XRD patterns do not show distinct reflections, which can be assigned to SiO_2, metallic Ga or Gallium oxides. This indicates such phases to be noncrystalline or liquid.[48] The absence of Ga-compounds in the X-ray patterns could be attributed to the formation of highly dispersed Ga_2O_3 species upon calcination, which are further reduced on the surface of the Pd at elevated temperatures. A similar mechanism has been suggested in ref 33, where Ga^{3+} species are claimed to be reduced on Pd nanoparticles by the highly active hydrogen atoms contained in the form of palladium hydride.

3.2.2. In Situ EXAFS. The XRD results described above reveal the formation of the $GaPd_2$ phase. EXAFS results capture the local structure and thus complement the knowledge of the catalyst gained from in situ XRD measurements. The protocol for catalyst activation is described in Section 2.3. Figure 4 shows the experimental and adjusted Fourier transform of the k^2-weighted EXAFS spectra of the catalyst at room temperature at the Pd K-edge (a) and Ga K-edge (b) after in situ reduction. The structural parameters obtained from the fitting procedure are presented in Table 1. The experimental and fitted data for $GaPd_2$ crystal structure are in good agreement, as the ρ factor is within the acceptable range.[49]

The crystallographic model shows that in the bulk structure of $GaPd_2/SiO_2$, Pd atoms are situated in two different sites: the average coordination numbers show that Pd is, on average, surrounded by 3.5 Ga atoms and by an outer shell of 5.5 Pd atoms. The refinement shows that the number of Ga atoms is smaller than expected for a bulk structure; this suggests that the $GaPd_2$ alloy is composed of small particles, supporting the XRD data. A coordination smaller than expected is found, since a significant fraction of Ga atoms are on the surface of the particle and have a reduced number of neighbors compared with the bulk. On the other hand, the coordination number refined for the second shell is slightly higher than the value expected for the bulk structure. In the case of Pd foil, the closest Pd neighbor is found at 2.76 Å. Under H_2 atmosphere, Pd nanoparticles can form Pd hydride, which causes the atomic distances to expand to 2.80 Å, as previously reported.[50] Hence, the higher coordination number found for the second shell of Pd in $GaPd_2$ might stem from the combination of the atomic distances of Pd atoms in the $GaPd_2$ structure with Pd hydride stemming from the 10% unalloyed fraction. Regarding the chemical environment of Ga, in the bulk structure, each Ga atom is surrounded by 10 Pd atoms located in two shells. The first shell is composed of 6 Pd atoms, located around 2.55 Å, whereas the second shell contains 4 Pd atoms located 2.61−2.95 Å from the Ga center. The absence of a significant second shell in the Fourier transformed spectrum (Figure 4b) can be attributed to its longer atomic distance, which decreases the amplitude of the EXAFS signal. This, combined with the broad spread of atomic distances (2.61−2.95 Å), might cause destructive interferences. Furthermore, the small particle size also contributes to the absence of higher shells because a significant fraction of the atoms are located on the surface (for a spherical $GaPd_2$ nanoparticle with a diameter of 12 nm, the fraction of surface atoms is ∼15%). The low R values found in the Fourier transform of the Ga K-edge spectra (Figure 4b) could be refined as oxygen scatterers; alternatively, these features might be related to low-frequency components of the EXAFS spectrum,

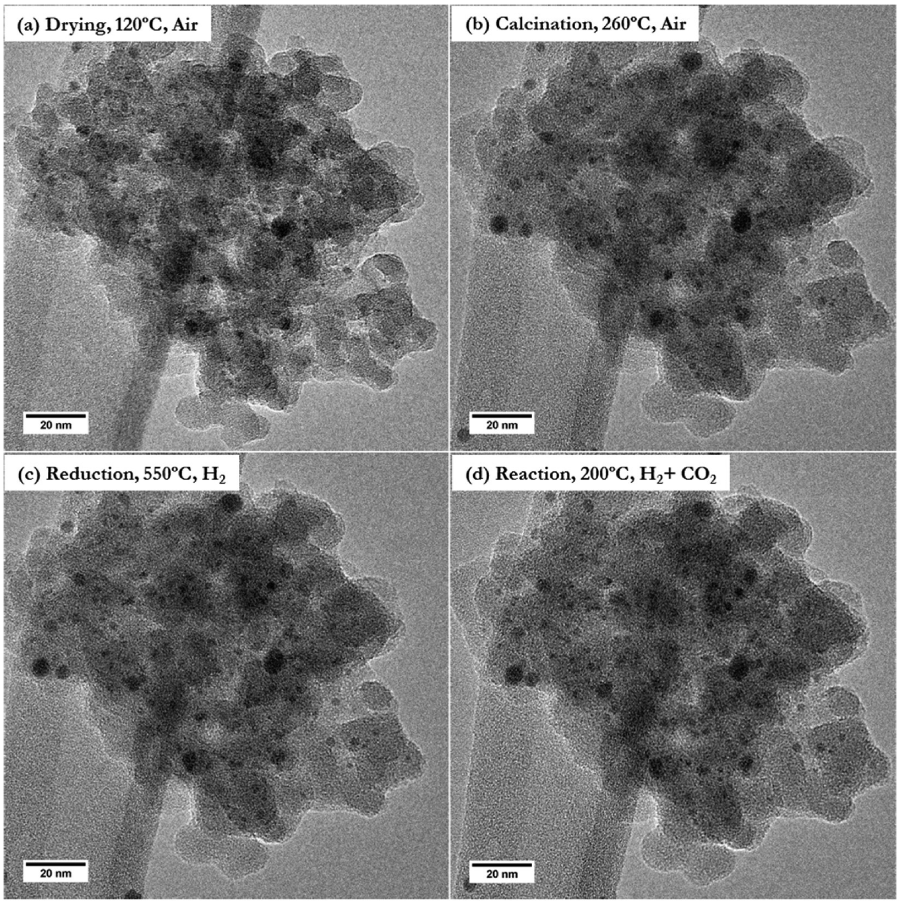

Figure 5. IL-TEM images of the $GaPd_2/SiO_2$ catalyst acquired after drying (a), calcination (b), reduction (c), and methanol synthesis (d).

which could not be removed during the background subtraction. A visualization of the first shell of the structural models used to refine the EXAFS is shown in the Supporting Information as Figure S3.

3.2.3. IL-TEM Results. TEM images of identical locations acquired according to the catalyst preparation and testing scheme procedure are shown in Figure 5. Nanoparticles on the SiO_2 support are observed after drying of the catalyst precursors (Figure 5a), in line with the XRD analysis, which shows that PdO nanocrystals are formed already at 120 °C. Previous reports suggest that thermal decomposition of $Pd(NO_3)_2$ to PdO starts above 100 °C. After calcination, partial sintering of the substrate is observed, as shown in Figure 5b. The nanoparticle size and dispersion are apparently determined during the calcination step because no significant changes in size and dispersion are observed after the reduction step (i.e., transformation of the PdO and Ga_2O_3 into $GaPd_2$, Figure 5c) and hydrogenation of CO_2 to methanol, Figure 5d.

Interestingly, agglomeration of the nanoparticles is not seen when the temperature is increased to 550 °C during the temperature-programmed reduction. This is in contrast to the sintering behavior of Pd/SiO_2: its dispersion decreases significantly with increasing reduction temperature.[51] The stability of the $GaPd_2$ nanoparticles toward agglomeration could be to a large extent attributed to the high degree of covalency of the metal−metal bonding in the intermetallic compounds.[52] A number of positions have been probed by IL-TEM approach, leading to the same conclusions.

A STEM image of an individual nanoparticle acquired after reduction is shown in Figure 6a, and the EDX line profile of the Pd-L and Ga-K signals across the particle is shown in Figure 6b. No segregation of Pd and Ga is observed, indicating that the bulk structure of the $GaPd_2$ nanoparticle is maintained after subsequent passivation and exposure of the catalyst to air, as was also shown in the in situ XRD experiment. This result is further confirmed by the analysis of high-resolution TEM images of individual nanoparticles. In Figure 6c,d an atomically resolved image and the corresponding FFT are shown, respectively, revealing the crystal structure of a $GaPd_2$ nanoparticle viewed along the [001] zone axis.

Some conclusions regarding nanoparticle dispersion can be drawn from Figure 5. First, nanoparticles of different sizes are present in the catalyst, suggesting that the dispersion could be further improved by optimizing the preparation method. Second, under reaction conditions, the structured of the catalysts are not visibly influenced, which could explain the catalytic stability of the $GaPd_2/SiO_2$.

3.2.4. ETEM Results. The development of the $GaPd_2/SiO_2$ catalyst has been further studied in situ by acquiring ETEM images and SAED patterns along the catalyst preparation and testing scheme at a total pressure of 4 mbar. The main purpose was to compare the results of the ETEM with those of the IL-TEM study described above to assess the pressure dependency on the active phase formation.

Images are shown in Figure 7 and indicate a similar evolution of the catalyst as observed in the IL-TEM images, acquired after ambient pressure treatment. In both cases, the nanoparticles'

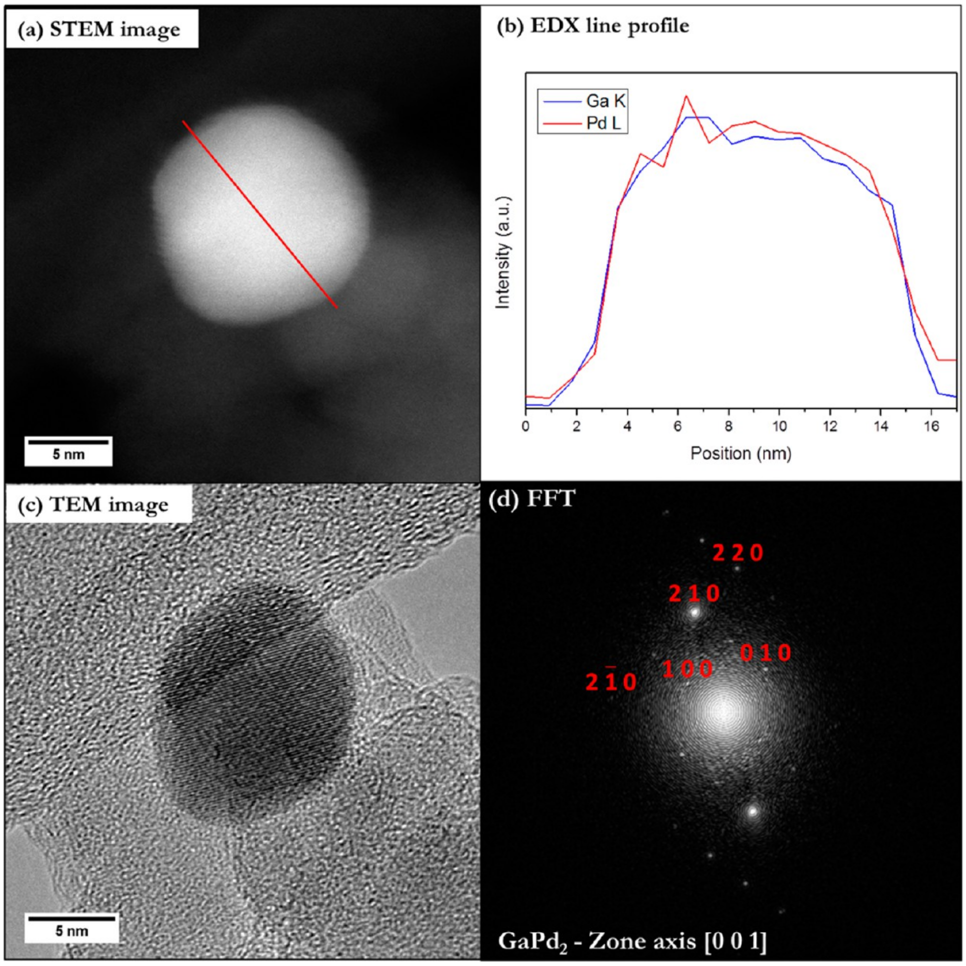

Figure 6. (a) STEM image of a $GaPd_2$ nanoparticle acquired after reduction. (b) EDX profile of Pd-L and Ga-K signals across the nanoparticle. (c) High resolution TEM image of a $GaPd_2$ nanoparticle acquired after reduction. (d) The corresponding fast Fourier transform (FTT).

sizes and dispersions are determined upon calcination, and no significant changes of these parameters are observed after reduction and methanol synthesis. Moreover, sintering of the support is also observed upon calcination. Both ETEM and IL-TEM images reveal the presence of nanoparticles in the range of 3−20 nm. In situ XRD data (Figure 3) suggest an average crystal size of $GaPd_2$ nanoparticles of 12 nm.

SAED patterns acquired under calcination and reduction conditions in the ETEM and corresponding radial intensity profiles are shown in Figure 8. Upon calcination, the PdO crystal phase is identified, and upon reduction, the $GaPd_2$ phase is formed. This indicates that under both ETEM and IL-TEM conditions, the route to the active phase formation is essentially the same, despite the significant difference in pressure. As a general rule, caution is needed when comparing information obtained at pressures that differ by a few orders of magnitude,[53,54] but in this work, ETEM and IL-TEM results can be correlated directly, just as SAED and XRD patterns can be. High-resolution images of individual nanoparticle are acquired under reduction conditions. An atomically resolved image is shown in Figure 9, revealing a crystal structure of a $GaPd_2$ nanoparticle in the [100] zone axis. Although XRD analysis reveals that under ETEM conditions, the sample should contain 15% metallic Pd, we have not observed pure Pd nanoparticles in the numerous high-resolution images acquired. Furthermore, the electron diffractograms do not allow concluding for the presence of additional metallic palladium after alloying formation because of the poorer sensitivity and resolution compared with the XRD patterns shown in Figure 2 and 3b.

4. DISCUSSION

The choice of SiO_2 as a support material in the present study is dictated by several considerations. First, it possesses a high surface area, which is important to achieve good dispersion of the catalyst nanoparticles. Second, SiO_2 is a convenient support for characterization purposes: it is XRD-amorphous (i.e. does not give reflections in the X-ray patterns), which could otherwise overlap with those of the supported nanoparticles. It is also a convenient material for microscopy studies, where again, the amorphous nature of SiO_2 facilitates the structural analysis of the supported nanoparticles while giving good contrast with $GaPd_2$ crystallites.

By coupling the Scherrer analysis of the XRD peaks to the catalytic data acquired by GC, it is found that the intrinsic activity (activity per unit surface of nanoparticles) is highest for the $GaPd_2/SiO_2$ system, when compared with the conventional $Cu/ZnO/Al_2O_3$. Moreover, the undesired rWGS activity is the lowest for the $GaPd_2$ catalyst, as shown in Figure 1. The size of the $GaPd_2$ crystallites is comparatively large (around 12 nm), implying that dispersion could be further improved. Using a lower loading of metals to get smaller $GaPd_2$ nanoparticles could be one way to optimize the content of the costly palladium.

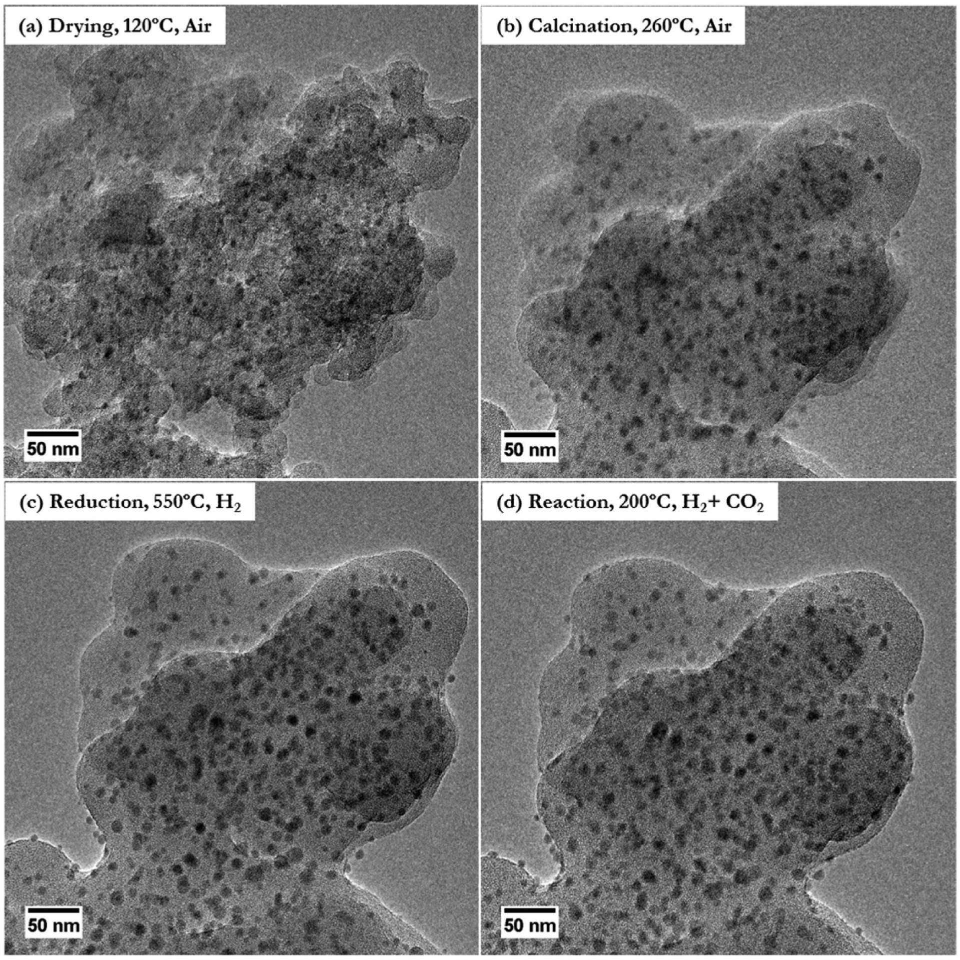

Figure 7. ETEM images of the $GaPd_2/SiO_2$ catalyst acquired after drying (a), calcination (b), reduction (c), and methanol synthesis (d).

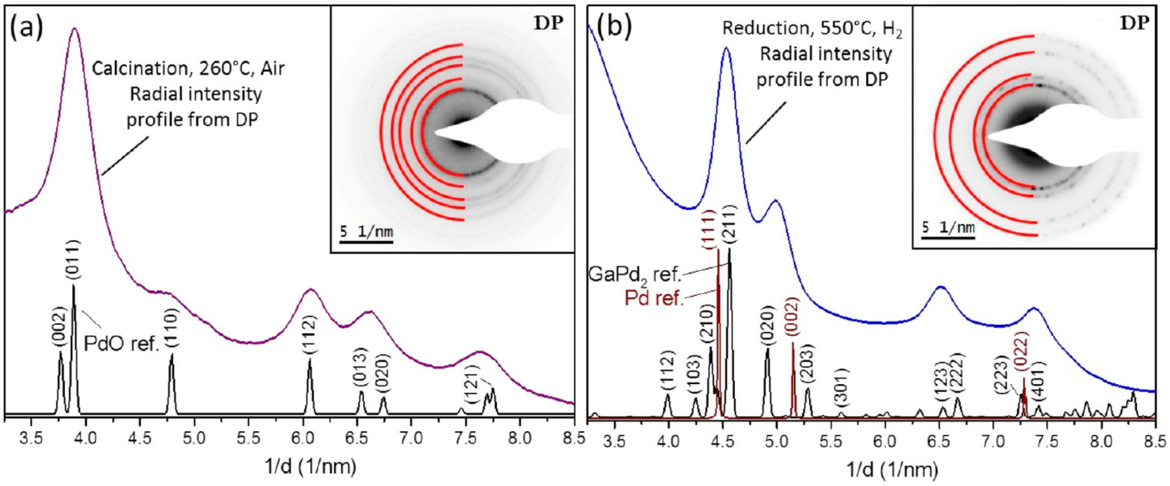

Figure 8. Intensity profiles from diffraction patterns in the insets acquired in the ETEM under calcination (a) and reduction (b) conditions. The references for PdO, metallic Pd, and $GaPd_2$ crystal phases are shown for comparison.

The stability of the catalyst has also been studied. The CO_2 hydrogenation reaction was carried out for 20 h at 200 °C, resulting in no loss of activity. This is consistent with the in situ XRD analysis, which reveals that the phase composition and the average crystal size of the catalyst remains stable after a similar test (Figure 3b). As confirmed by IL-TEM (Figure 5) and ETEM (Figure 7), the dispersion of the nanoparticles is not affected by exposure to reaction conditions. The stability of the active surface is another prerequisite for stable conversion, and the results clearly indicate that neither surface nor bulk structures are altered during the reaction.

As seen from Figure 2, metallic palladium is present in the catalyst after preparation. Although some authors[23] suggest that the unalloyed Pd could be responsible for the rWGS reaction,

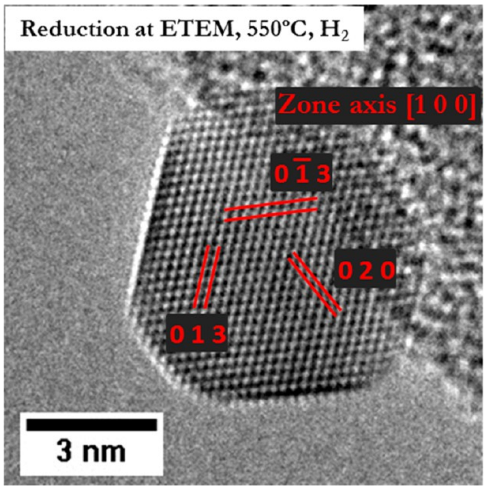

Figure 9. High-resolution TEM image of a $GaPd_2$ nanoparticle acquired in the ETEM under reduction conditions (550 °C, 4 mbar H_2).

others believe[22,25] that metallic palladium alone is barely active toward rWGS. The ability to reduce CO_2 to CO under methanol synthesis conditions could thus be attributed to $GaPd_2$. To the best of our knowledge, the ability of phase-pure $GaPd_2$ nanoparticles or individual surfaces to convert CO_2 to CO under methanol synthesis conditions has not been investigated.

In situ XRD and EXAFS reveal the local and the long-range crystal structure of the catalysts along the catalyst preparation and testing scheme. XRD suggests that 4 nm PdO crytallites evolve into 12 nm $GaPd_2$, which at first glance points toward temperature-induced sintering upon reduction/alloying at 550 °C. However, both IL-TEM and ETEM analysis shows that the size of the nanoparticles does not change significantly during the transformation from PdO precursor to $GaPd_2$ catalyst (Figure 5 and 7). This could imply that the PdO nanoparticles observed after the calcination step consist of polycrystallites, which form a bigger Pd crystallite upon exposure to H_2 and later evolve into single crystalline $GaPd_2$ nanoparticles during the temperature-programmed reduction.

In general, calcination is often a required step in catalyst preparation. It is necessary to decompose some of the components of the precursor to allow solid-state reaction between components, redistribute the active species, or to enhance the porous structure.[55] For example, calcination of the $Cu/ZnO/Al_2O_3$ precursor is essential because of the formation of the metastable amorphous hydrocarbonates and aurichalcite that finally lead to formation of a very active catalyst.[56] On the other hand, in some cases, direct reduction is known to result in a more active catalyst. The examples include $Cu{-}Ni/SiO_2$ for high pressure CO hydrogenation[57] and $Ni{-}Ga/SiO_2$ for CO_2 hydrogenation.[21] In the present case, calcination is apparently important to anchor the PdO nanocrystals to the SiO_2 support, as suggested by electron microscopy analysis.

In general, this work highlights the benefits of utilizing a combination of complementary characterization tools to reveal the structure of a catalyst and propose ways to improve catalytic properties. Moreover, development of a methodology for studying the catalyst both under realistic (atmospheric pressure) and ETEM (up to 20 mbar) pressure, as well as validating that the complementary results obtained under different conditions are directly comparable, has been a major part of this work. By studying the evolution of the catalyst during the catalyst preparation and testing scheme both under ambient and ETEM pressure, and by combinational analysis of the results obtained from XRD, EXAFS, IL-TEM, and ETEM, we have concluded that the path to formation of the $GaPd_2/SiO_2$ catalyst from metal nitrates is similar, irrespective of the pressure. This implies that further investigations of the catalyst under in situ ETEM conditions could, for example, shed light on the structure of the surface during methanol synthesis reaction and correlate it with the catalytic activity observed at atmospheric pressure. In situ characterization of the catalyst prepared directly in the environmental microscope, using techniques such as HRTEM, EDX, and SAED, confirms that the desired $GaPd_2$ phase is formed.

5. CONCLUDING REMARKS AND OUTLOOK

The central topic of this work has been synthesis, catalytic testing, and characterization of $GaPd_2/SiO_2$ intermetallic catalysts for hydrogenation of CO_2 to methanol at ambient pressure. It has been shown that $GaPd_2/SiO_2$ prepared by impregnation of metal nitrates and consecutive reduction is a promising catalyst for CO_2 hydrogenation to methanol in terms of activity, selectivity, and stability. The catalyst could be further optimized in terms of reduction temperature and metal loading, with the aim of obtaining a more phase pure catalyst. Suppressing the CO production to achieve an even better selectivity is also an important optimization step, should the catalyst be considered for industrial applications.

The evolution of the catalyst along the catalyst preparation and testing scheme has been investigated by a combination of ex situ and in situ characterization techniques such as XRD, EXAFS, ETEM, and IL-TEM. This enabled us to study the different aspects of the catalysts structure under both ambient and ETEM conditions. It has been shown that the “pressure gap” in this study is bridged, that is, there is a good correlation between the results obtained at different pressures. This opens up possibilities for deeper investigations of the catalyst under in situ TEM conditions to gain more insights into the dynamic changes during methanol synthesis reaction and directly correlate them to the catalytic activity measured in a plug-flow reactor under atmospheric pressure.

The approach of combining complementary characterization tools has proved to be a comprehensive and powerful method for studying the Pd−Ga catalysts for CO_2 hydrogenation to methanol, and we believe that the developed methodology might be applicable for a wide range of catalyst.

■ ASSOCIATED CONTENT

Ⓢ Supporting Information

The Supporting Information is available free of charge on the ACS Publications website at DOI: 10.1021/acscatal.5b01271.

Equilibrium considerations and additional information on stability and structure of the catalysts (PDF)

■ AUTHOR INFORMATION

Corresponding Author

*E-mail: e.fiordaliso@cen.dtu.dk.

Notes

The authors declare no competing financial interest.

■ ACKNOWLEDGMENTS

The Center for Individual Nanoparticle Functionality is sponsored by The Danish National Research Foundation (DNRF54). The A.P. Møller and Chastine Mc-Kinney Møller

Foundation is gratefully acknowledged for the contribution toward the establishment of the Center for Electron Nanoscopy at the Technical University of Denmark. The authors are grateful to Soleil Synchrotron for granting beamtime at SAMBA beamline and to Dr. Valerie Briois for her assistance during the measurements.

REFERENCES

(1) Ganesh, I. *Renewable Sustainable Energy Rev.* **2014**, *31*, 221−257.
(2) Wasmus, S.; Kuver, A. *J. Electroanal. Chem.* **1999**, *461*, 14−31.
(3) Yaripour, F.; Baghaei, F.; Schmidt, I.; Perregaard, J. *Catal. Commun.* **2005**, *6*, 147−152.
(4) Fu, Y. C.; Hong, T.; Chen, J. P.; Auroux, A.; Shen, J. Y. *Thermochim. Acta* **2005**, *434*, 22−26.
(5) Haw, J. F.; Marcus, D. M. *Top. Catal.* **2005**, *34*, 41−48.
(6) Song, W. G.; Marcus, D. M.; Fu, H.; Ehresmann, J. O.; Haw, J. F. *J. Am. Chem. Soc.* **2002**, *124*, 3844−3845.
(7) Hutchings, G. J.; Van Rensburg, L. J.; Copperthwaite, R. G.; Hunter, R.; Dwyer, J.; Dewing, J. *Catal. Lett.* **1990**, *4*, 7−14.
(8) Waugh, K. C. *Catal. Today* **1992**, *15*, 51−75.
(9) Campbell, C. T.; Daube, K. A.; White, J. M. *Surf. Sci.* **1987**, *182*, 458−476.
(10) Bowker, M.; Hadden, R. A.; Houghton, H.; Hyland, J. N. K.; Waugh, K. C. *J. Catal.* **1988**, *109*, 263−273.
(11) Grunwaldt, J. D.; Molenbroek, A. M.; Topsøe, N.-Y.; Topsøe, H.; Clausen, B. S. *J. Catal.* **2000**, *194*, 452−460.
(12) Hansen, P. L.; Wagner, J. B.; Helveg, S.; Rostrup-Nielsen, J. R.; Clausen, B. S.; Topsøe, H. *Science* **2002**, *295*, 2053−2055.
(13) Rasmussen, P. B.; Holmblad, P. M.; Askgaard, T.; Ovesen, C. V.; Stoltze, P.; Norskov, J. K.; Chorkendorff, I. *Catal. Lett.* **1994**, *26*, 373−381.
(14) Sun, J. T.; Metcalfe, I. S.; Sahibzada, M. *Ind. Eng. Chem. Res.* **1999**, *38*, 3868−3872.
(15) Twigg, M. V.; Spencer, M. S. *Appl. Catal., A* **2001**, *212*, 161−174.
(16) Kurtz, M.; Wilmer, H.; Genger, T.; Hinrichsen, O.; Muhler, M. *Catal. Lett.* **2003**, *86*, 77−80.
(17) Olah, G. A.; Prakash, G. K. S.; Goeppert, A. *J. Am. Chem. Soc.* **2011**, *133*, 12881−12898.
(18) Chen, L.; Jiang, Q.; Song, Z.; Posarac, D. *Chem. Eng. Technol.* **2011**, *34*, 817−822.
(19) Liu, X. M.; Lu, G. Q.; Yan, Z.F.; Beltramini, J. *Ind. Eng. Chem. Res.* **2003**, *42*, 6518−6530.
(20) Studt, F.; Sharafutdinov, I.; Abild-Pedersen, F.; Elkjaer, C. F.; Hummelshoj, J. S.; Dahl, S.; Chorkendorff, I.; Norskov, J. K. *Nat. Chem.* **2014**, *6*, 320−324.
(21) Sharafutdinov, I.; Elkjaer, C. F.; Pereira de Carvalho, H. W.; Gardini, D.; Chiarello, G. L.; Damsgaard, C. D.; Wagner, J. B.; Grunwaldt, J. D.; Dahl, S.; Chorkendorff, I. *J. Catal.* **2014**, *320*, 77−88.
(22) Fujitani, T.; Saito, M.; Kanai, Y.; Watanabe, T.; Nakamura, J.; Uchijima, T. *Appl. Catal., A* **1995**, *125*, L199−202.
(23) Ota, A.; Kunkes, E. L.; Kasatkin, I.; Groppo, E.; Ferri, D.; Poceiro, B.; Navarro, R. M.; Yerga; Behrens, M. *J. Catal.* **2012**, *293*, 27−38.
(24) Collins, S. E.; Delgado, J. J.; Mira, C.; Calvino, J. J.; Bernal, S.; Chiavassa, D. L.; Baltanas, M. A.; Bonivardi, A. L. *J. Catal.* **2012**, *292*, 90−98.
(25) Kong, H.; Li, H. Y.; Lin, G. D.; Zhang, H. B. *Catal. Lett.* **2011**, *141*, 886−894.
(26) Chiavassa, D. L.; Collins, S. E.; Bonivardi, A. L.; Baltanas, M. A. *Chem. Eng. J.* **2009**, *150*, 204−212.
(27) Klanjsek, M.; Gradisek, A.; Kocjan, A.; Bobnar, M.; Jeglic, P.; Wencka, M.; Jaglicic, Z.; Popcevic, P.; Ivkov, J.; Smontara, A.; Gille, P.; Armbrüster, M.; Grin, Y.; Dolinsek, J. *J. Phys.: Condens. Matter* **2012**, *24*, 085703.
(28) Wowsnick, G.; Teschner, D.; Kasatkin, I.; Girgsdies, F.; Armbrüster, M.; Zhang, A. P.; Grin, Y.; Schlogl, R.; Behrens, M. *J. Catal.* **2014**, *309*, 209−220.
(29) Li, L. D.; Zhang, B. S.; Kunkes, E.; Fottinger, K.; Armbrüster, M.; Su, D. S.; Wei, W.; Schlogl, R.; Behrens, M. *ChemCatChem* **2012**, *4*, 1764−1775.
(30) He, Y. F.; Liang, L. L.; Liu, Y. N.; Feng, J. T.; Ma, C.; Li, D. Q. *J. Catal.* **2014**, *309*, 166−173.
(31) Lorenz, H.; Thalinger, R.; Kock, E. M.; Kogler, M.; Mayr, L.; Schmidmair, D.; Bielz, T.; Pfaller, K.; Klotzer, B.; Penner, S. *Appl. Catal., A* **2013**, *453*, 34−44.
(32) Shao, L.; Zhang, W.; Armbrüster, M.; Teschner, D.; Girgsdies, F.; Zhang, B.; Timpe, O.; Friedrich, M.; Schloegl, R.; Su, D. S. *Angew. Chem., Int. Ed.* **2011**, *50*, 10231−10235.
(33) Armbrüster, M.; Wowsnick, G.; Friedrich, M.; Heggen, M.; Cardoso-Gil, R. *J. Am. Chem. Soc.* **2011**, *133*, 9112−9118.
(34) Leary, R.; de la Pena, F.; Barnard, J. S.; Luo, Y.; Armbrüster, M.; Meurig Thomas, J.; Midgley, P. A. *ChemCatChem* **2013**, *5*, 2599−2609.
(35) Baltes, C.; Vukojevic, S.; Schüth, F. *J. Catal.* **2008**, *258*, 334−344.
(36) Grunwaldt, J. D.; van Vegten, N.; Baiker, A. *Chem. Commun.* **2007**, *44*, 4635−4637.
(37) Ravel, B.; Newville, M. *J. Synchrotron Radiat.* **2005**, *12*, 537−541.
(38) Kovnir, K.; Schmidt, M.; Waurisch, C.; Armbrüster, M.; Prots, Y.; Grin, Y. *Z. Kristallogr.−New Cryst. Struct.* **2008**, *223*, 7−8.
(39) Rehr, J. J.; Kas, J. J.; Prange, M. P.; Sorini, A. P.; Takimoto, Y.; Vila, F. *C. R. Phys.* **2009**, *10*, 548−559.
(40) Mayrhofer, K. J. J.; Ashton, S. J.; Meier, J. C. G.; Wiberg, K. H.; Hanzlik, M.; Arenz, M. *J. Power Sources* **2008**, *185*, 734−739.
(41) Schlogl, K.; Hanzlik, M.; Arenz, M. *J. Electrochem. Soc.* **2012**, *159*, B677−B682.
(42) Thune, P. C.; Weststrate, C. J.; Moodley, P.; Saib, A. M.; van de Loosdrecht, J.; Miller, J. T.; Niemantsverdriet, J. W. *Catal. Sci. Technol.* **2011**, *1*, 689−697.
(43) Hansen, T. W.; Wagner, J. B.; Dunin-Borkowski, R. E. *Mater. Sci. Technol.* **2010**, *26*, 1338−1344.
(44) Waser, J.; Levy, H. A.; Peterson, S. W. *Acta Crystallogr.* **1953**, *6*, 661−663.
(45) Owen, E. A.; Yates, E. L. *Philos. Mag.* **1933**, *15*, 472−488.
(46) Friedrich, M.; Teschner, D.; Knop-Gericke, A.; Armbrüster, M. *J. Phys. Chem. C* **2012**, *116*, 14930−14935.
(47) Koizumi, N.; Jiang, X.; Kugai, J.; Song, C. *Catal. Today* **2012**, *194* (1), 16−24.
(48) Armbrüster, M.; Cardoso-Gil, R. *Z. Anorg. Allg. Chem.* **2015**, *641*, 1453−1458.
(49) Calvin, S. *XAFS for Everyone*; CRC Press: Boca Raton, FL, 2013, 305.
(50) Grunwaldt, J. D.; Caravati, M.; Hannemann, S.; Baiker, A. *Phys. Chem. Chem. Phys.* **2004**, *6*, 3037−3047.
(51) Ryndin, Y. A.; Stenin, M. V.; Boronin, A. I.; Bukhtiyarov, V. I.; Zaikovskii, V. I. *Appl. Catal.* **1989**, *54*, 277−288.
(52) Armbrüster, M.; Grin, Y.; Schloegl, R. *Complex Metallic Phases in Catalysis*; Wiley-VCH: Weinheim, 2011, 386.
(53) Jaeger, N. I. *Science* **2001**, *293* (5535), 1601−1602.
(54) Topsøe, H. *J. Catal.* **2003**, *216*, 155−164.
(55) Pernicone, N.; Traina, F. *Pure Appl. Chem.* **1978**, *50*, 1169−1191.
(56) Bems, B.; Schur, M.; Dassenoy, A.; Junkes, H.; Herein, D.; Schlogl, R. *Chem.—Eur. J.* **2003**, *9*, 2039−2052.
(57) Wu, Q. X.; Eriksen, W. L.; Duchstein, L. D. L.; Christensen, J. M.; Damsgaard, C. D.; Wagner, J. B.; Temel, B.; Grunwaldt, J. D.; Jensen, A. D. *Catal. Sci. Technol.* **2014**, *4*, 378−386.